



Strengthening of DBA substrate with Ni/Ti/Ag metallization for thermal fatigue-resistant Ag sinter joining in GaN power modules

Dongjin Kim^{1,2} · Chuantong Chen² · Seung-Joon Lee³ · Shijo Nagao² · Katsuaki Suganuma²

Received: 2 December 2019 / Accepted: 17 January 2020 / Published online: 23 January 2020
© Springer Science+Business Media, LLC, part of Springer Nature 2020

Abstract

This study was carried out to develop a DBA (direct bonded aluminum) substrate with Ni/Ti/Ag metallization to achieve highly functional thermal shock stability of Ag sinter joining in GaN (Gallium Nitride) power modules. GaN/DBA die-attached module structures by Ag sinter joining was performed during harsh thermal shock cycling tests within a temperature range of $-50/250$ °C. In the case of DBA without a Ni metallization layer (Ti/Ag), severe degradation occurred at the interface between the sintered Ag and Al due to significant plastic deformation of the Al layer. The shear strength decreased from an initial value of 33.1 MPa to 22.3 MPa after 500 cycles. With EBSD investigation, it was determined that the Al layer underwent sub-grain rotation recrystallization during thermal shock cycles. This led to a non-uniform grain orientation distribution at center and corner locations. On the other hand, Ni/Ti/Ag metallization showed that it can prevent severe Al deformation due to the superior rigidity achieved by Ni metallization. The die-shear strength maintained almost the same value as its initial value, even after 500 cycles. In addition, a numerical simulation analysis determined that the Ag sinter joining structure on the DBA substrate with Ni/Ti/Ag metallization had high functionality in stress relaxation. This study provided a novel approach to design thermal shock stability Ag sinter joining for next-generation power modules in high-temperature applications.

1 Introduction

Power semiconductors are a key component to enable efficient power distribution, usage, and generation for electric driving systems [1]. To further improve energy efficiency, wide band-gap (WBG) semiconductors such as silicon carbide (SiC) and gallium nitride (GaN) are emerging in various fields for use in future electronic devices and components [2–4]. These WBG semiconductors theoretically allow power electronic devices to be operated at significantly higher temperatures (> 250 °C) and at higher power density and with higher frequency switching than traditional silicon (Si)-based power devices (< 150 °C) [5–7].

In particular, GaN devices are expected to play a significant role in improving the performance of in-wheel motors or on-board charger (OBC) in environmentally friendly vehicles such as electric vehicles (EV) due to their high-frequency operation characteristics (10–100 GHz) [8]. The main feature of these WBG devices is their stability when operated at significant high temperature, which can ultimately be effective in reducing the weight and volume of overall power conversion systems by eliminating the need for large and heavy heat dissipation systems [9–11]. However, to implement effective operation of the WBG devices at over 250 °C, other module components like interconnections, insulators, and heat-dissipating substrates also must possess such stability in harsh operating environments [12]. In addition, due to direct contact of materials with different coefficients of thermal expansion (CTE), the assembled components are subjected to thermo-mechanical stress with repetitive switching [13–15].

With the implementation and promotion of the Restriction of Hazardous Substances directive (RoHS), the use and application of lead in many industry products has become problematic [15]; nevertheless, high-content lead solders are still pending in the RoHS regulations [16–18].

✉ Chuantong Chen
chenchuantong@sanken.osaka-u.ac.jp

¹ Department of Adaptive Machine Systems, Graduate School of Engineering, Osaka University, Suita-shi, Osaka 565-0871, Japan

² The Institute of Scientific and Industrial Research, Osaka University, Ibaraki-shi, Osaka 567-0047, Japan

³ Department of Advanced Materials Engineering, Korea Polytechnic University, Siheung 15073, Republic of Korea

For this reason, many lead-free solder studies have been developed. Sn-based lead-free solders are unlikely to operate normally above 250 °C due to their low melting point [19, 20]. Moreover, the cost of Au–Sn-based solders is quite high compared with other candidates [21, 22]. In this context, Ag sinter joining is attracting most attention as a low-temperature bonding material (< 300 °C) and a low-pressure bonding material (< 1 MPa) [23]. Sintered Ag joints maintain stability at temperatures above 300 °C due to their high melting point of about 960 °C [24]. Additionally, sintered Ag joints offer high thermal and electrical conductivity, much higher than that of traditional solder materials [24, 25]. However, pressure-less/low-temperature bonding of Ag sintering technology and the reduction of overall cost remain an industry issue [23, 26]. Therefore, developing a low-cost Ag paste for low-temperature, pressure-less sintering has generated active research and is a current challenge in this field [27].

Another issue for high-power electronics is the heat dissipation/insulation substrate. Direct bonded copper (DBC) and a direct bonded aluminum (DBA) are widely using in industry [28]; however, several studies have reported that DBC was unreliable due to the problem of Cu diffusion and oxidation at the high temperature [29]. Also, with regard to DBA, it has been reported that plastic-deformed Al is accompanied by the recrystallization of the Al of the DBA substrate due to harsh temperatures [30]. This deformation behavior and mechanism are still not entirely clear, but they are key to a long-term reliability reduction factor. Thus, die-attached materials that can withstand high temperatures (> 250 °C) and also the development of high-performance heat dissipation/insulation substrates without experiencing oxidation and diffusion are key advancements required for the implementation of next-generation high-reliability power modules [31].

To overcome comprehensive problems such as performance reliability, pricing, and material design (including the above-mentioned issues for WBG power device applications), the reliability of the integrated structure of chips, bonding materials, and substrates should be evaluated. Our research group applied pressure-less and low-temperature hybrid Ag sinter joining and Ni metallization design on the DBA substrate to a GaN die-attached power module structure. The GaN/DBA die-attached structure was subjected to harsh thermal shock testing at a temperature range of – 50 to 250 °C for a duration of up to 500 cycles. The shear strength, microstructure evolution, and fracture characteristics were evaluated by shear tester, FE-SEM, EDX, and EBSD observation, respectively. In this study, we intensively examined the relationship between microstructural behavior and mechanical strength of the Al layer of the DBA with Ni layer and without Ni layer in experimentally and numerically.

2 Material and method

2.1 Preparation of hybrid Ag sinter paste

Figure 1a, b shows micron Ag flakes and submicron Ag particles, respectively. The Ag submicron particles (FHD, Mitsui Mining and Smelting Co., Ltd, Japan) and the micron Ag flakes (AgC239, Fukuda Metal Foil and Powder, Kyoto, Japan) were mixed as Ag fillers of hybrid Ag sinter paste in a weight ratio of 1:1. The micron Ag flakes and submicron Ag particles were stirred magnetically for 10 min and vibrated ultrasonically for 30 min in alcohol. Finally, they were mixed with an ether-type solvent (CELTOL-IA, Daicel Corporation) using a mixer (HM-500, Keyence Corporation) to make the hybrid Ag paste into a uniform mixture. The amount of solvent was maintained at approximately 10 wt% in the paste to keep a suitable viscosity of 150–250 cPs at room temperature (RT).

2.2 Metallization and pressure-less Ag sinter joining

Figure 1c displays GaN/DBA die-attached module structure and its depiction of each layer. Dummy grade GaN die (5 mm × 5 mm × 0.5 mm) was introduced for bonding to the DBA substrate (Al/AlN/Al). In the case of the Ni metallized DBA, 200 nm Ti and 2 μm Ag were sputtered on the back side of the GaN die, and then 7 μm Ni, 200 nm Ti, and 2 μm Ag were sequentially sputtered on the top side of the DBA substrates. In the case of the non-Ni metallized DBA case, the above process was followed, yet the 7 μm Ni sputtering process on the DBA was excluded. For the Ag sintering, the pressure-less sintering was realized by using a temperature profile of 250 °C for 30 min in air as shown in Fig. 1d.

2.3 Thermal shock test and characterization

For the thermal shock reliability evaluation, a thermal shock chamber (TSE-11-A-S, ESPEC, Osaka, Japan) was employed. Evolution of the microstructures and mechanical properties were investigated before and after thermal shock tests at temperature range from – 50 °C to 250 °C for 30 min in each extreme temperature up to 500 cycles. The specimens subjected to thermal shock cycle test were then shear tested. The bonding strength of the GaN/DBA joints was evaluated by shear tester machine (DAGE 4000 bonds tester, UK) at a speed of 50 μm/s. The cross-section of Ag sinter joints was prepared by an ion-milling polishing machine (IM4000, Hitachi, Tokyo, Japan), and the microstructure characteristic was observed by a field-emission scanning electron microscopy (FE-SEM, SU8020, Hitachi, Tokyo, Japan), energy-dispersive X-ray

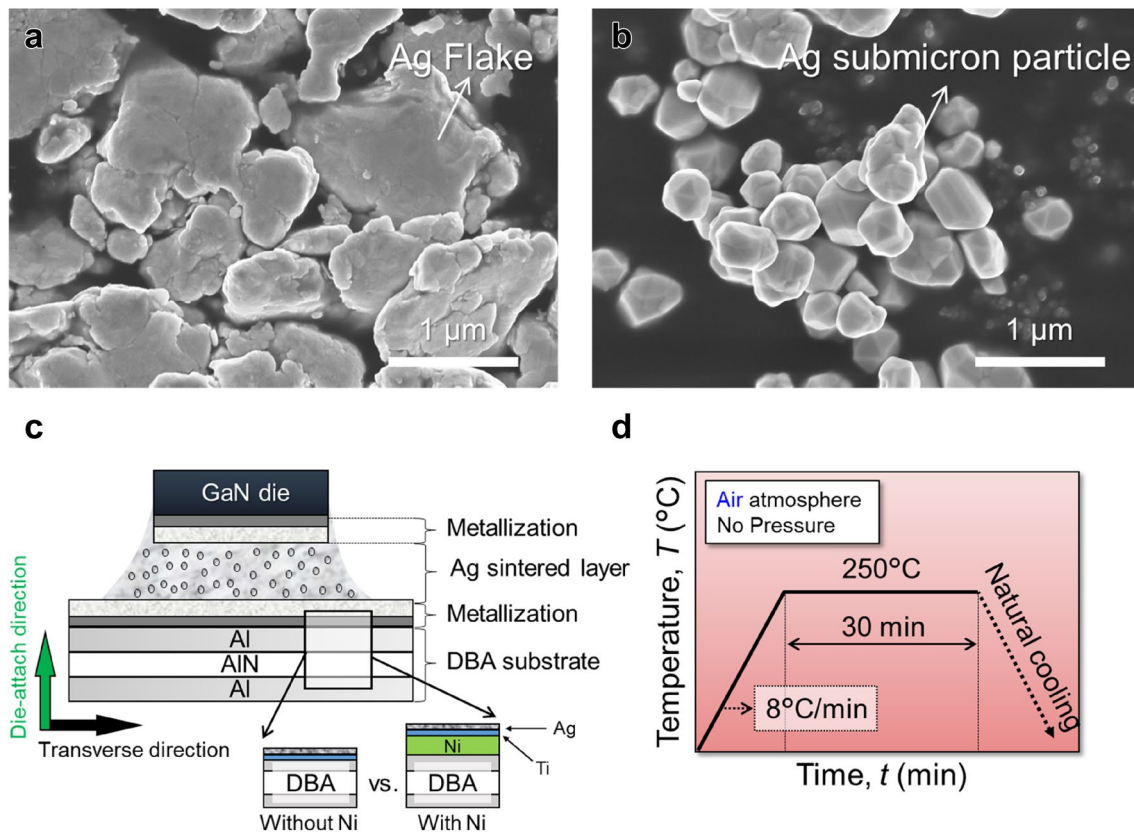


Fig. 1 **a** Micron Ag flakes, **b** submicron Ag particles, **c** GaN/DBA die-attached module structure and its description of layers, and **d** low-temperature and pressure-less Ag sinter joining condition in air

spectroscopy (EDX), and electron backscatter diffractometer (EBSD; EDAX-TSL, Hikari).

2.4 Numerical simulation model

To understand the Ni layer effect of GaN/DBA die-attached module structures, thermo-mechanical finite element method (FEM) simulation was performed using the commercial finite element program ANSYS. Interfaces of Ag–Al with Ni layer and without Ni layer examined grain boundaries for analysis models for conceptual designed as shown in Fig. 2a. Material properties were applied for thermal elastic–plastic analysis as shown in Table 1. The boundary conditions were applied with the actual thermal shock cycling condition of one cycle as displayed in Fig. 2b.

3 Results

3.1 Bonding strength

Shear strength is a key indicator for reliability assessment of the bonding structure. Figure 3 exhibits the relationship

between shear strength and the number of thermal shock cycles. When a GaN/DBA die-attached assembly is subjected to a harsh thermal shock environment, strength evolution depends on the metallization design. Shear strength of the non-Ni metallized specimen gradually reduced at 125 cycles, and it was significantly reduced by 33% after 500 cycles of thermal shock (see blue color line). On the other hand, in the case of Ni metallized specimens, they sustained their shear strength at initial strength for up to 500 cycles (see red color line). Surprisingly, shear stress reduction was substantially suppressed by Ni metallization. The key factor of this strength reduction and strength sustention of the joints will be discussed in the next section.

3.2 Microstructure characteristics

Figure 4 shows cross-section images of an Ag sinter joint before and after thermal shock cycles. The tendencies of interface behavior differed substantially between those joints with an Ni metallization layer and those without a Ni metallization layer. Figure 4a exhibits a GaN Ag sinter bonded structure without a Ni layer. The initial state formed a structurally sound micro-Ag porous joint as shown in

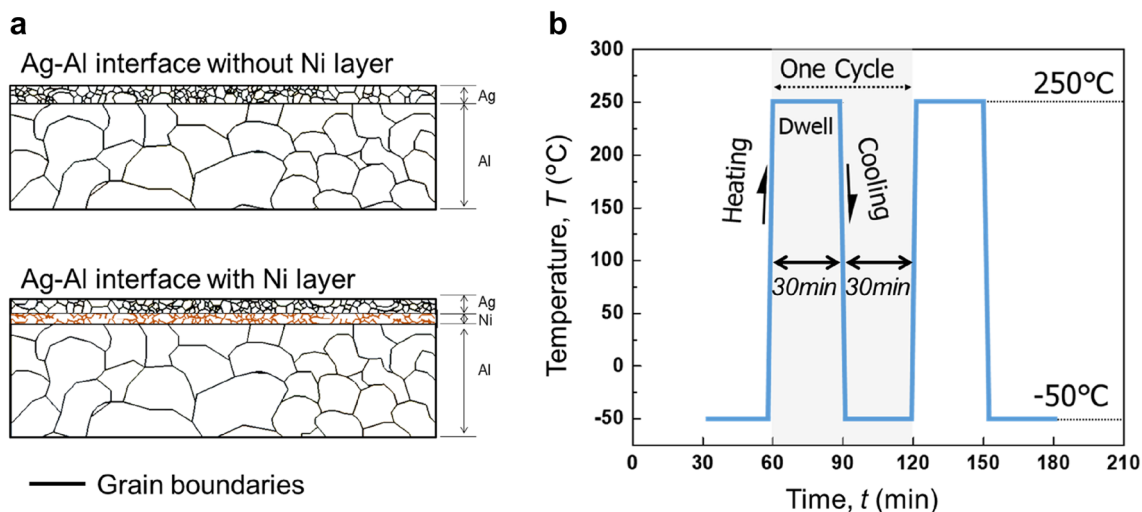


Fig. 2 a Analysis models of Ag–Al interfaces. b Temperature profile for FE simulation

Table 1 Material properties for FEM simulation

Material	Density (kg/m ³)	CTE (K ⁻¹)	Thermal Conductivity (W/mK)	Young's modulus (GPa)	Poisson's ratio	Plasticity (MPa)
Ag paste	6294	19.2×10^{-6}	430	12.9	0.1	6000
Al	2700	25.7×10^{-6}	137	70	0.33	10,000
Ni	8900	13.4×10^{-6}	90.9	200	0.31	–

Fig. 3 Relationship between die-shear strength and thermal shock cycle number. Blue color line is non-Ni metallization specimen and red color line is Ni metallized specimen (Color figure online)

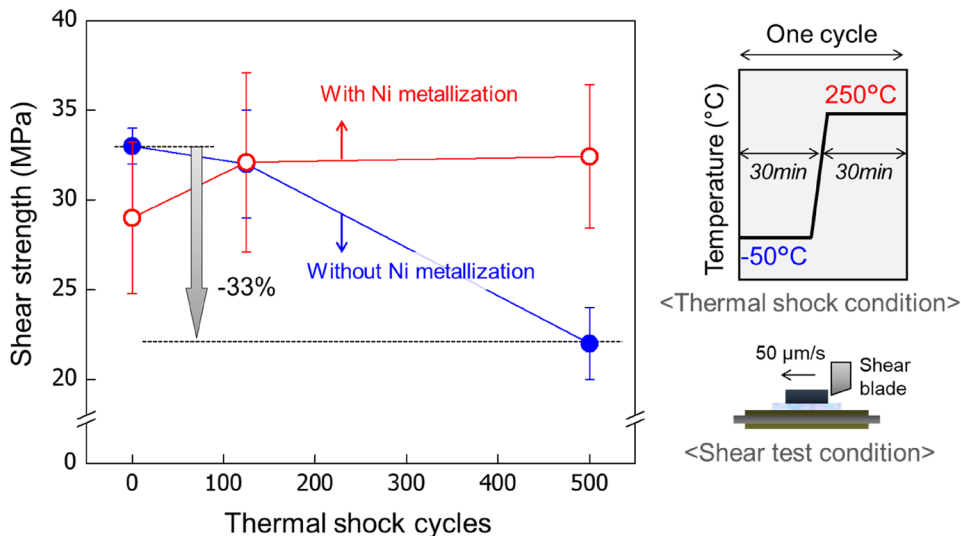


Fig. 4a₁. On the other hand, along the yellow line, the interface between the sintered Ag layer and Al of the DBA can be clearly seen after 500 cycles (see Fig. 4a₂). In the case of the Ni metallized GaN, the die-attached structure also successfully bonded micro-porous Ag structure by pressure-less Ag sintering process as displayed in Fig. 4b₁. In addition, the Ag–Al interface sustained like initial state after 500 cycles

(see Fig. 4b₂). In the process, the Ag neck was somewhat thicker, but no deformation defects were found, and the Ni metallized specimen suggests a substantially improved interfacial reliability than those of the non-Ni metallized specimens due to suppressed plastic deformation of the Al layer by the Ni sputtered layer. Thus, through cross-sectional SEM observations, it is clearly seen that the most predominant

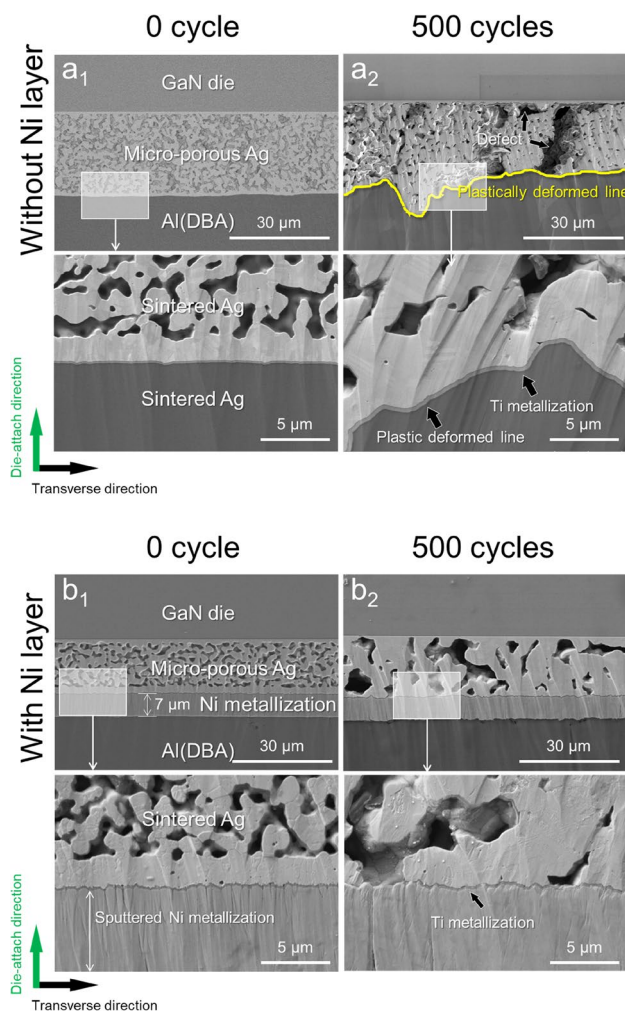


Fig. 4 Microstructure evolution images before and after thermal shock cycles. Cross-section images of the with Ni metallized GaN/DBA die-attached structure by thermal shocks **a**₁ as-bonded without Ni layer, **a**₂ 500 cycles without Ni layer, and **b**₁ as-bonded with Ni layer, **b**₂ 500 cycles with Ni layer

factor in strength reduction and sustention can be attributed to an interface deformation between the Ag sintered layer and the Al layer.

3.3 Fracture surface

To observe how an interfacial deformation affects fracture, a fracture surface analysis of both types of metallized GaN die-attached structures was conducted after 500 cycles as shown in Fig. 5. Again, using both die-attached structures (those with an Ni Layer and those without), it was determined that initial fractures occurred in the Ag sinter joints. The interfacial behavior of the two trends analyzed in the cross-sectional SEM observations had a significant effect on the change of the fracture surface. In the case of those without a Ni layer, a roughened fractured surface is shown in

Fig. 5a. Figure 5b displays a high magnification image of the Fig. 5a, and it can be clearly seen that a porous structure is on the roughened surface. In addition, the roughened surface is composed of Al element and the porous structure composed of the Ag element, as determined by EDX mapping analysis (see Fig. 5c). Therefore, in the case of those without a Ni layer, it is explained that an interfacial failure induced delamination at the Ag–Al interface during shear tests due to the plastic-deformed interface. On the other hand, in the case of those with an Ni layer, an overall flat fracture surface was observed (see Fig. 5d). Under high magnification imaging, a plate-like fragment, which is regarded as metallization layer off the chip, was observed as shown in Fig. 5e. As was determined by EDX element mapping analysis, fragments regarded as a metallization layer were found to consist of the Ti element; the main element of the fracture surface was found to be Ag element. No Al element was detected at all (see Fig. 5f). Namely, the entire fracture path is inside the Ag sinter joint and the Ag sinter joint remained virtually unchanged from its initial state. This indicates that the fracture occurred at the Ag sinter joint, as in its initial state without any interface degradation. Therefore, the change of fracture path before and after thermal shocks can be summarized by Fig. 6.

4 Discussions

4.1 Roughness of Al surface

To investigate the effect of the Ni layer on the deformation of the interface of Ag–Al by thermal shocks, a surface roughness measurement of Al was performed using a laser microscope. Figure 7 shows the results of the roughness measurement of the Al surface of the DBA. The initial state of the Al surface showed no noticeable surface roughness in SEM observation (see Fig. 7a). In addition, no significant roughening was observed by laser scanning, and a maximum roughness of about 3 μm was quantified by 3D analysis as shown in Fig. 7b, c. Figure 7d exhibits the case of Al surface without Ni layer, showing severe roughness on the Al surface with wrinkled areas and cracks clearly detected. In addition, for the Al surface without Ni layer, the height difference was found to have increased from the initial state (see Fig. 7e). As shown in Fig. 7f, the maximum roughness was about 50 μm as quantified by 3D analysis. Formation of an Al hillock is attributed to the occurrence of surface roughness, and it has been reported that the Al hillock is caused by atomic diffusion due to stress migration (SM) and thermal fatigue (TF) during repetitive thermal cycling [32]. Finally, in the case of Al surface with an Ni layer, the SEM image shows no noticeable surface roughness

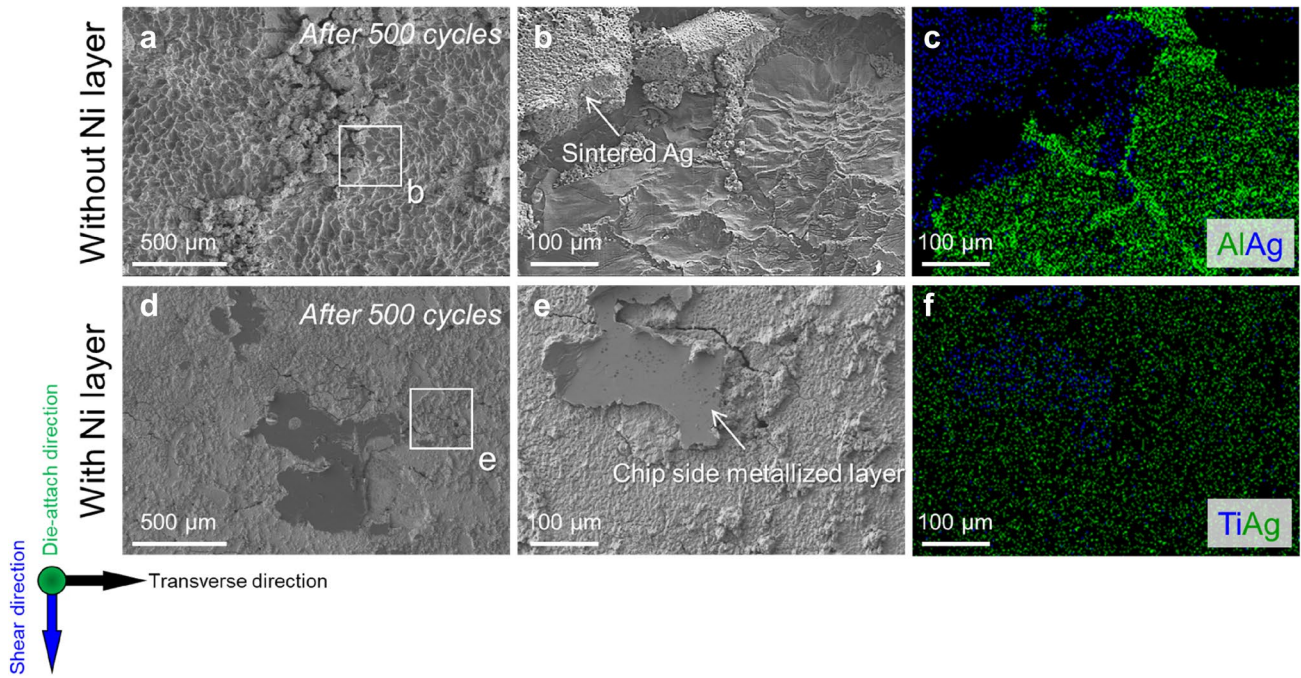
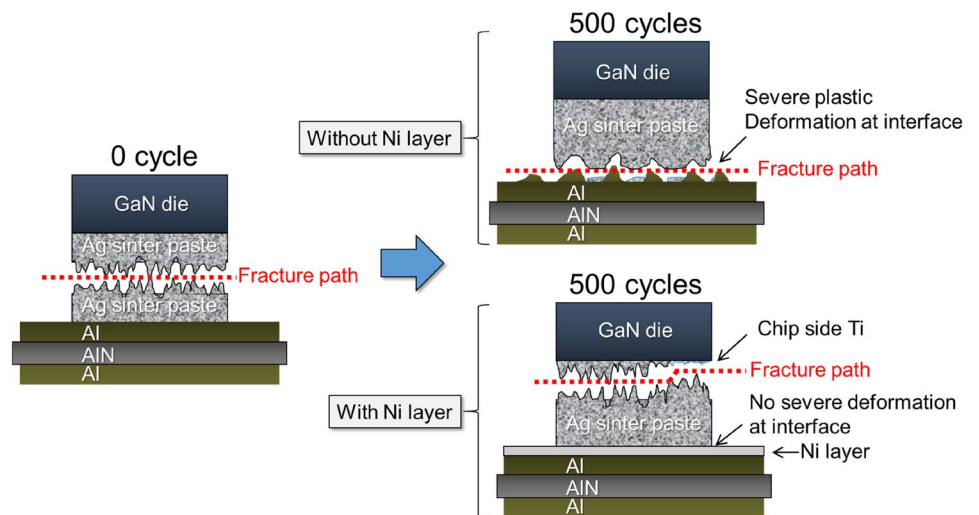


Fig. 5 Fracture surface analysis results after 500 cycles. **a** fractured surface image of the non-Ni sample of, **b** its high magnification image, **c** EDX elements' mapping result, **d** fractured surface of the

Ni metallized sample, **e** its high magnification image, and **f** EDX elements' mapping result

Fig. 6 Schematic description of fracture path change



nor cracking. Figure 7h,i shows a similar tendency of the roughness of Al surface to remain as in its initial state. Thus, it has been found that the Ni layer plays a role in the prevention of cracking on the metallized DBA surface by suppressing the deformation behavior of Al during thermal shock cycling. The changing grain characteristics are discussed in detail in the next section.

4.2 Grain characteristics of Al and Ni layer

To further understand the relationship between the deformation behavior of the Al layers and the grain characteristics, EBSD analysis was conducted. The accelerating voltage, probe current, working distance, step size, and minimum confidence index (CI) for the EBSD analysis were 20 kV,

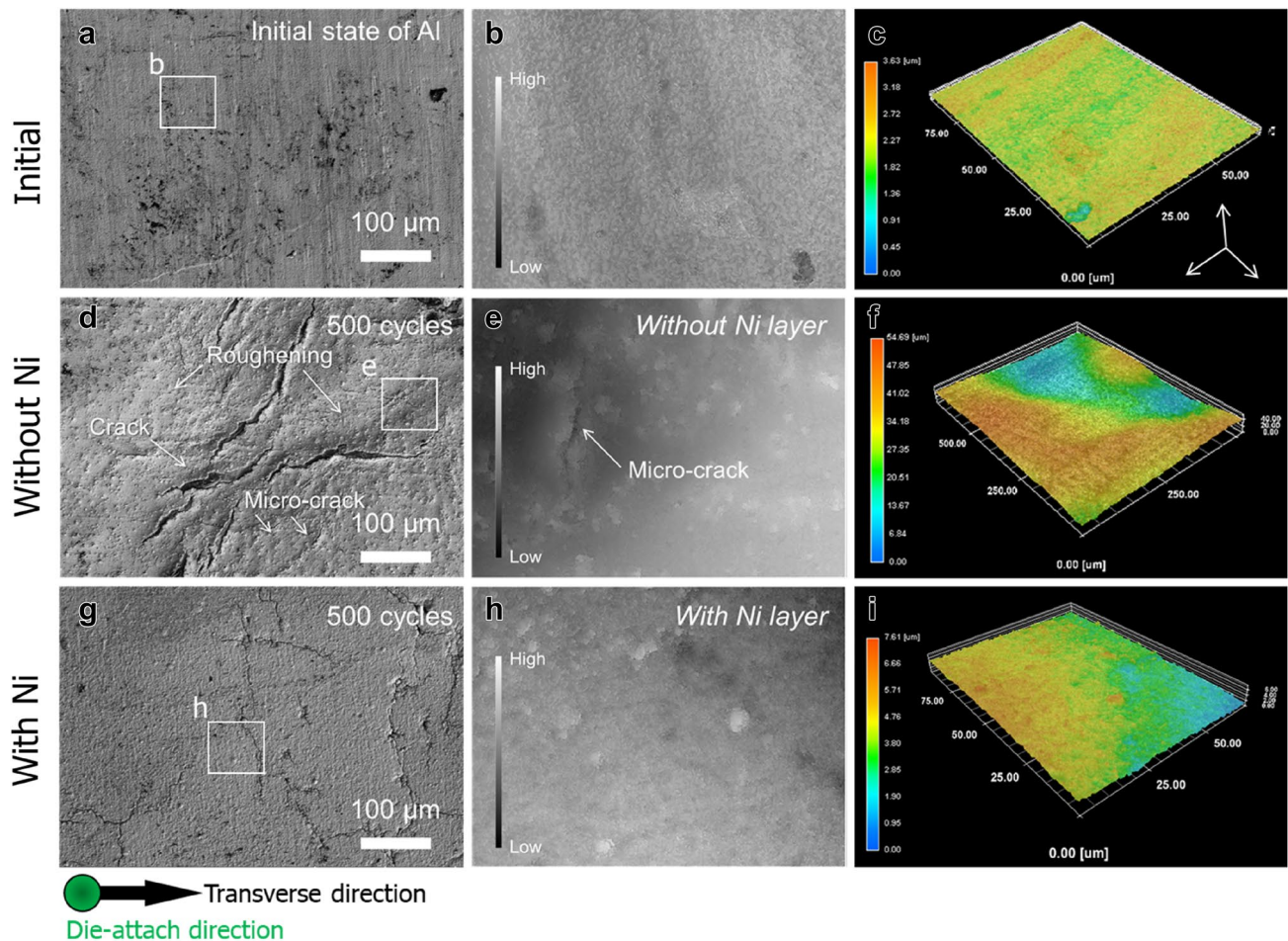


Fig. 7 Results of roughness measurement of Al surface of DBA. **a** SEM image of initial state roughness of Al surface, **b** its laser scanning area, **c** 3D roughness measurement result of **(b)**, **d** SEM image of Al surface of without Ni layer after 500 cycles, **e** its laser scanning

area, **f** 3D roughness measurement result of **(e)** and **(g)** Al surface of with Ni layer after 500 cycles, **h** its laser scanning area, and **i** 3D roughness measurement result of **(h)**

12 nA, 15 mm, 0.025 (1) μm , and 0.1, respectively, for the Ni (Al) layers. To measure the deformation-induced local misorientation, the kernel average misorientation (KAM) value was calculated up to the 2nd neighbor shell with a maximum misorientation angle of 5° using the TSL-OIM software. Figure 8 exhibits EBSD observation results of the cross-sectional Al layer, where the observations were performed at the die-attached center and at the corner where maximum stress occurred. Figure 8a shows the inverse pole figure (IPF) map; the orientation of the initial state of Al layers was (001) at both center and corner. After 500 cycles, the Al grain orientation was significantly different depending on the presence of a Ni layer. In the case of Al without the Ni layer, the central orientation distribution is almost (001) direction, and the grain orientation distribution at the corner was changed from its initial red color to yellow color unlike center. However, in the case of Al with the Ni layer, grain orientation distributions of the center and corner showed

a similar tendency (similar color distributions). Then, IPF change tendency is displayed in Fig. 8b, after 500 cycles, the grain orientation distributions in the center are green color and the grain orientation distributions in the corners are black color. Here, Al without Ni layer exhibits different grain orientation distribution developed at center and corner. Thus, it was found that the surface was severely deformed when the grain orientation distributions of the center and the corner were not similar. The change of grain boundary distributions is displayed in Fig. 8c. Low-angle grain boundaries (LAGBs, $2^\circ < \theta < 15^\circ$) are shown in red line and the high-angle grain boundaries (HAGBs, $15^\circ < \theta$) are shown in blue line. Initial state of the grain boundary distribution of Al layer was only LAGBs and large grain at the center and corner. However, after 500 cycles, all the cases have occurred a sub-grain rotation recrystallization inside Al layer by repetitive mechanical forces with thermal shock cycles. In particular, Al with Ni layer generated HAGBs more than did

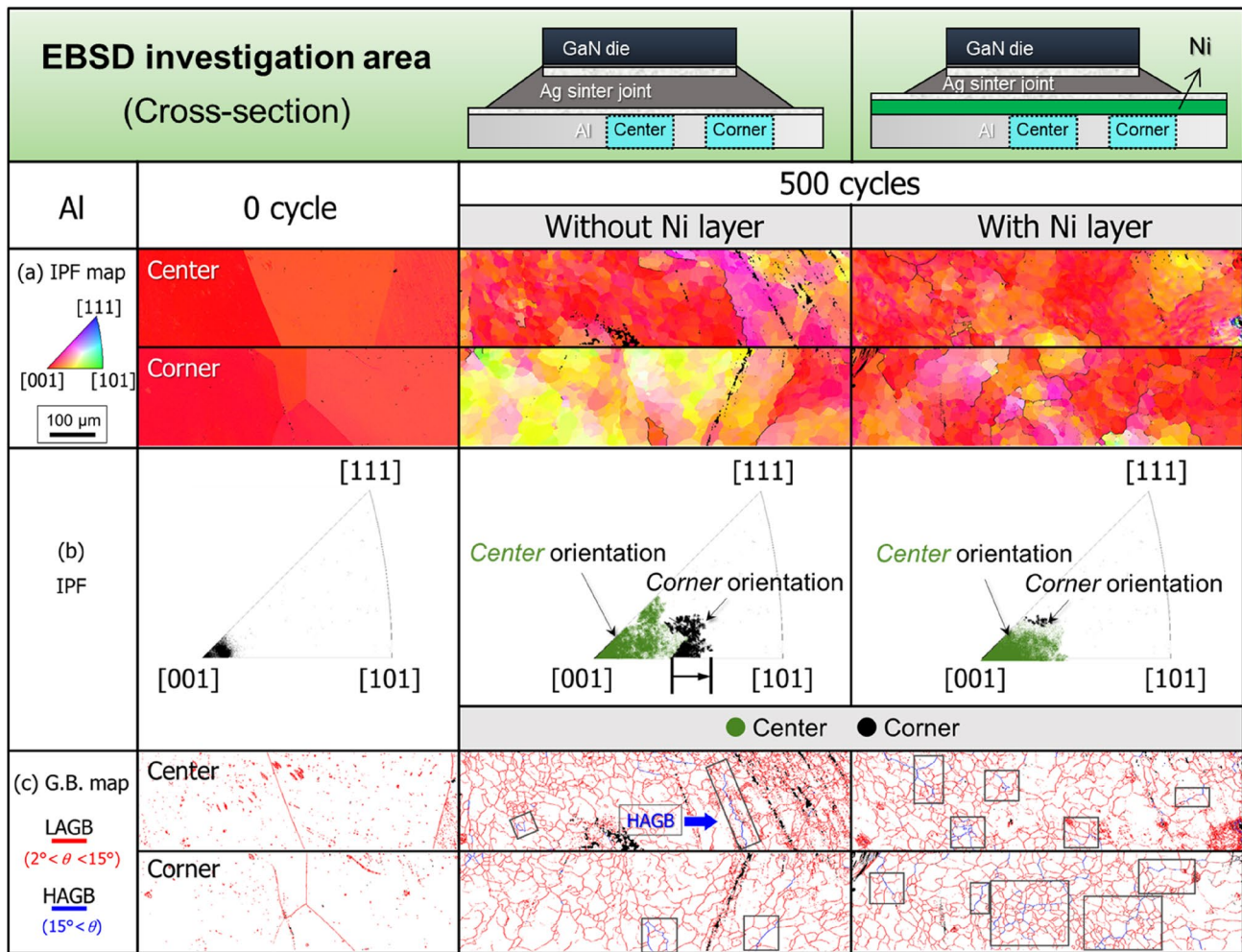


Fig. 8 EBSD observation results of cross-section of Al layer (DBA): **a** inverse pole figure map, **b** its IPF distribution, and **c** its grain boundaries map (Color figure online)

the Al without Ni layer. This sub-grain rotation recrystallization was due to the relationship between the energy versus the number of dislocations at the grain boundary where there is a driving force for fewer HAGBs to form and grow instead of a higher number of LAGBs [33, 34]. In addition, previous studies have reported that recrystallized grains can lead to improved yield strength [35], which makes deformation more difficult. Therefore, Al with a Ni layer is expected to be more difficult to display plastic deformation as the thermal shock cycle increases because the grain boundary develops into HAGBs while deformation is suppressed. Inconsistencies in the grain orientation of the center and corners have been found to cause severe deformation of the surface.

When the deformation of Al was suppressed, the grain characteristic change of the Ni was also analyzed by EBSD analysis. Figure 8 shows grain characteristic analysis results of the sputtered Ni layer before and after thermal shock cycles. As shown in Fig. 9a, no significant physical defects

were observed before and after the thermal shock cycle, and grain characteristics were analyzed for the white square box area. Figure 9b displays IPF maps showing that grain orientations were randomly distributed before and after thermal shock cycles. Grain size showed no significant change before and after thermal shock cycles. Figure 9c exhibits grain boundary distributions of the Ni layer before and after thermal shock cycles: low-angle grain boundaries (LAGBs, $2^\circ < \theta < 15^\circ$) are shown in red line and the high-angle grain boundaries (HAGBs, $15^\circ < \theta$) are shown in the blue line. HAGBs formed from as-sintered state, without significantly change after thermal shock cycles, and its quantitative misorientation angle distribution plotting is displayed in Fig. 9d. The kernel average misorientation (KAM) maps are drawn using an average misorientation angle around a measurement point with respect to a defined set of the nearest neighbor points with a maximum misorientation angle of 3° . The KAM values were under 1° before and after thermal shock

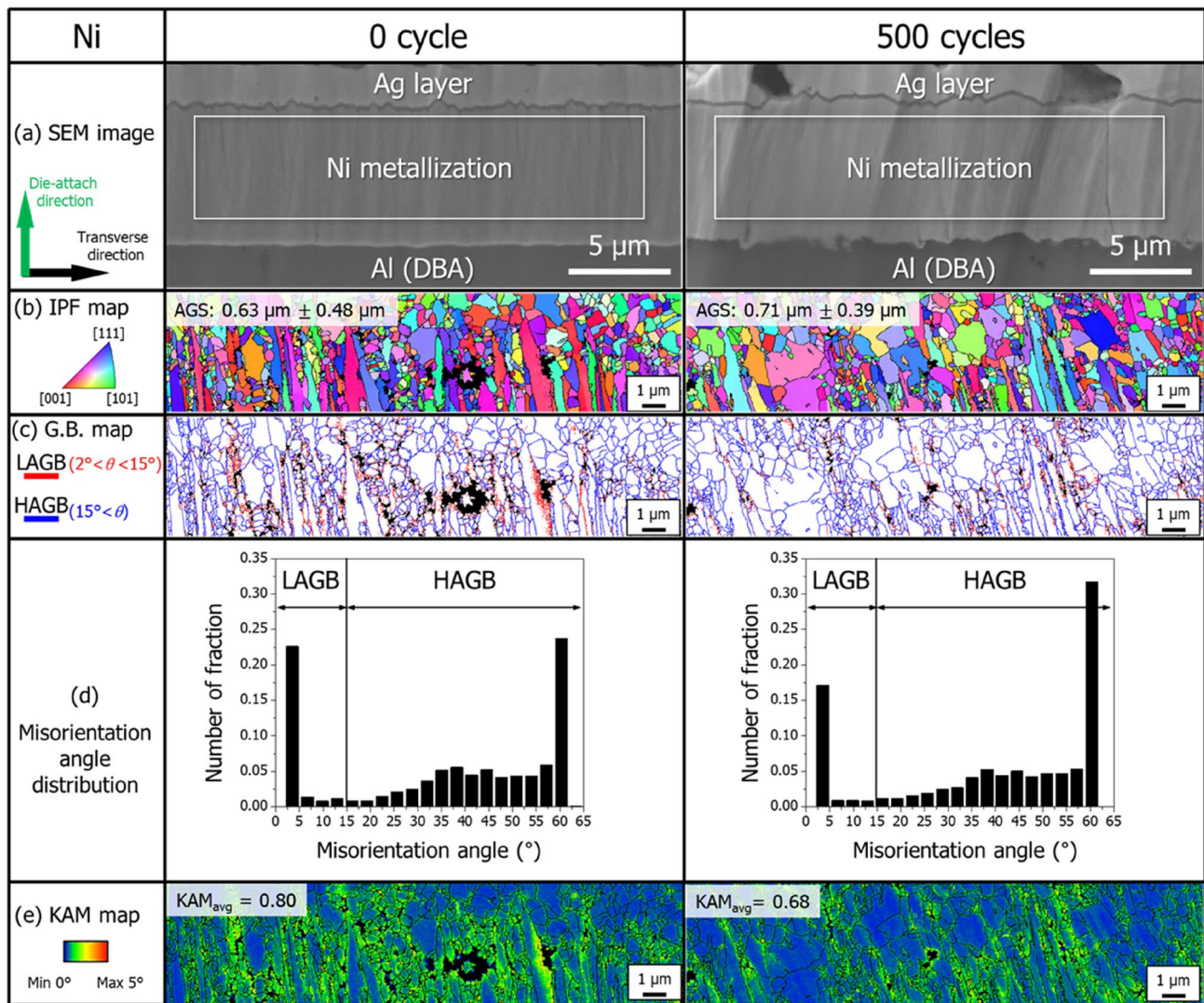


Fig. 9 Grain characteristics analysis results of the sputtered Ni layer before and after thermal shocks. **a** SEM images, **b** inverse pole figure (IPF) maps, the red lines denote low-angle boundaries with misorientation angles between 2° and 15°, and the blue lines denote high-

angle boundaries with misorientation angles exceeding 15°. **c** grain boundaries maps and **d** misorientation angle distribution, **e** kernel average misorientation (KAM) maps (Color figure online)

cycles. Since the KAM values of both cases were as low as ~1.0, the effect of thermal shock cycles were considered insignificant. Therefore, the Ni layer is not considered to be critically stressed by thermal shock and is believed to play a role in stress relaxation.

4.3 Stress behavior verification by FEM simulation

To verify the effect of Ni to suppression of Al deformation, a finite element method (FEM) simulation was introduced. For thermal–mechanical simulation, EBSD information based on FE modeling of Ag–Al layers was performed as displayed in Fig. 10a. The Ag sinter paste and Al are assumed to have elastic–plastic properties to reveal deformation behavior. In this

process, to shorten the time and converge the calculation, the 200 nm Ti layer, which serves as a diffusion barrier, was not considered in the FEM simulation. The boundary conditions are applied with the actual thermal shock cycling condition of one cycle. Figure 10b shows the stress distribution of non-Ni layer model at 250 °C, it was confirmed that the stress concentration occurred around the Al grain boundaries by a thermal stress. The thermal stress induced a maximum stress at the interface between Ag and Al, and the results show a similar tendency with actual degradation SEM images (see Fig. 10c). Therefore, deformation mechanism of the Al without Ni layer can be explained by Fig. 10d. Namely, as the thermal stress acts on Al grain boundaries, the grains deform, and sintered Ag does not resist the Al deformation. Grains are then pushed

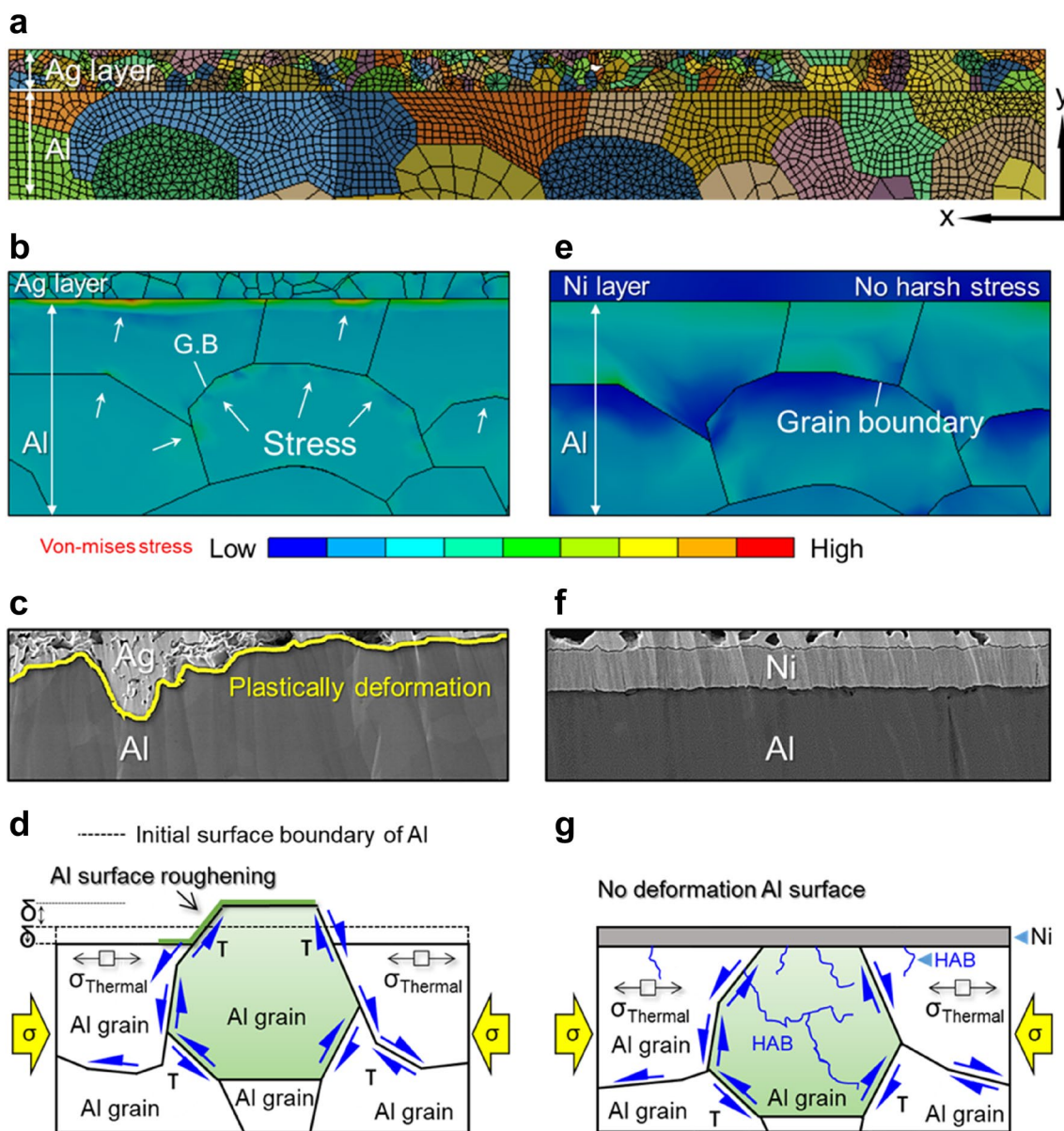


Fig. 10 FEM simulation result; description of mechanical behavior of Al–Ag interface without Ni layer and with Ni layer. **a** FE modeling of Ag–Al interface of analysis models, **b** stress distribution of non-Ni model at 250 °C, **c** actual degradation SEM image without Ni layer, **d**

its schematic description of deformation mechanism, **e** stress distribution of Ni model at 250 °C, **f** its actual SEM image with Ni layer, **g** Al surface roughing suppression mechanism by Ni layer

up on the surface, such as the initial dotted line, resulting in an uneven Ag–Al interface. On the other hand, compared with the non-Ni model, the Ni model has a lower intensity of the stress concentration in the Al grain boundaries. In particular, the Ni layer produced significantly lower stresses with its rigid property and demonstrated simulation results that correspond to the EBSD-KAM (Fig. 9e) results as shown in Fig. 10e. Also, the stress-simulated results exhibit a similar tendency with actual SEM observation images as shown in Fig. 10f. Consequently, as shown in Fig. 10d, Al grains tend to rise to the surface as a result of thermal stress; however, the Ni layer, having excellent

mechanical properties, suppresses the deformation behavior of the Al grains and the forces not consumed in the deformation are understood to contribute to the formation of HAGBs as displayed in Fig. 10g.

5 Conclusions

In the present work, a Ni metallization influence to suppress Ag–Al interfacial deformation of a GaN/DBA die-attached module structure in harsh thermal cycling (– 50 to 250 °C)

was examined in detail by means of microstructural observation and numerical simulation. A GaN/DBA die-attached module was stably sustained without physical degradation during thermal shock cycles by Ni metallization. In the case of a DBA without a Ni layer, strength reduced with Ag–Al interface deformation by 33% after 500 cycles. In the case of a DBA with an Ni layer, the shear strength of the joint structure sustained above initial strength after 500 cycles due to the suppression of the Ag–Al interface deformation by the Ni metallization layer during repetitive thermal shock cycles. In this process, both DBA generated sub-grain boundary rotation recrystallization, which becomes a driving force of surface roughening during thermal shock cycling. In the case of Al without Ni layer, grain orientation distributions were different between center and corner. On the other hand, in the case of Al with Ni layer, grain orientations were similarly distributed between center and corner and were also accompanied by many high-angle grain boundaries (HAGBs). In particular, the Ni layer showed no significant changes before and after harsh thermal shock cycles; thus, the thermal stress generated can be relaxed because the Ni layer does not physically react to harsh thermal shock cycles. Consequently, thick Ni metallization suppresses the surface roughness of Al layer caused by the sub-grain rotation recrystallization behavior of Al, thereby preventing strength reduction. This study systematically discussed the interfacial reliability of GaN/DBA die-attached module structures that change with the presence of the Ni metallization.

Acknowledgements This work was supported by the JST Advanced Carbon Technology Research and Development Program (ALCA) project “Development of a high frequency GaN power module package technology” (Grant No. JPMJAL1610). The author is thankful to the Network Joint Research Centre for Materials and Devices, Dynamic Alliance for Open Innovation Bridging Human, Environment, and Materials.

References

1. J. Millan, P. Godignon, X. Perpina, A. Perez-Tomas, J. Rebollo, A survey of wide bandgap power semiconductor devices. *IEEE Trans. Power Electron.* **29**, 2155–2163 (2014). <https://doi.org/10.1109/TPEL.2013.2268900>
2. H. Okumura, Present status and future prospect of widegap semiconductor high-power devices. *Jpn. J. Appl. Phys.* **45**, 7565 (2006). <https://doi.org/10.1143/JJAP.45.7565>
3. F. Roccaforte, F. Giannazzo, F. Iucolano, J. Eriksson, M.H. Weng, V. Raineri, Surface and interface issues in wide band gap semiconductor electronics. *Appl. Surf. Sci.* **256**, 5727–5735 (2010). <https://doi.org/10.1016/j.apsusc.2010.03.097>
4. F. Roccaforte, P. Fiorenza, G. Greco, R. Lo Nigro, F. Giannazzo, F. Iucolano, M. Saggio, Emerging trends in wide band gap semiconductors (SiC and GaN) technology for power devices. *Microelectron. Eng.* **187–188**, 66–77 (2018). <https://doi.org/10.1016/j.mee.2017.11.021>
5. F. Roccaforte, P. Fiorenza, G. Greco, M. Vivona, R. Lo Nigro, F. Giannazzo, A. Patti, M. Saggio, Recent advances on dielectrics technology for SiC and GaN power devices. *Appl. Surf. Sci.* **301**, 9–18 (2014). <https://doi.org/10.1016/j.apsusc.2014.01.063>
6. T. Ueda, Reliability issues in GaN and SiC power devices, in: 2014 IEEE International Reliability Physics Symposium (2014), pp. 1–6. <https://doi.org/10.1109/IRPS.2014.6860629>
7. Y. Yamada, Y. Takaku, Y. Yagi, I. Nakagawa, T. Atsumi, M. Shirai, I. Ohnuma, K. Ishida, Reliability of wire-bonding and solder joint for high temperature operation of power semiconductor device. *Microelectron. Reliab.* **47**, 2147–2151 (2007). <https://doi.org/10.1016/j.microrel.2007.07.102>
8. A. Pérez-Tomás, A. Fontserè, M. Placidi, M.R. Jennings, P.M. Gammon, Modelling the metal–semiconductor band structure in implanted ohmic contacts to GaN and SiC. *Model. Simul. Mater. Sci. Eng.* **21**, 035004 (2013)
9. H.S. Chin, K.Y. Cheong, A.B. Ismail, A review on die attach materials for SiC-based high-temperature power devices. *Metall. Mater. Trans. B* **41**, 824–832 (2010). <https://doi.org/10.1007/s11663-010-9365-5>
10. K.Y. Wong, W. Chen, X. Liu, C. Zhou, K.J. Chen, GaN smart power IC technology. *Phys. Status Solidi Basic Res.* **247**, 1732–1734 (2010). <https://doi.org/10.1002/pssb.200983453>
11. A.A. Bajwa, Y. Qin, R. Reiner, R. Quay, J. Wilde, Assembly and packaging technologies for higher temperature and high-power GaN devices. *IEEE Trans. Compon. Packag. Manuf. Technol.* **5**, 1402–1416 (2015). <https://doi.org/10.1109/TCPMT.2015.2468595>
12. C. Choe, C. Chen, S. Noh, Thermal shock performance of DBA/AMB substrates plated by Ni and Ni-P layers for high-temperature applications of power device modules. *Materials* **11**, 2394 (2018). <https://doi.org/10.3390/ma11122394>
13. S.H. Chen, P.C. Chou, S. Cheng, Evaluation of thermal performance of packaged GaN HEMT cascode power switch by transient thermal testing. *Appl. Therm. Eng.* **98**, 1003–1012 (2016). <https://doi.org/10.1016/j.applthermaleng.2015.12.110>
14. R. Kisiel, Z. Szczepański, Die-attachment solutions for SiC power devices. *Microelectron. Reliab.* **49**, 627–629 (2009). <https://doi.org/10.1016/j.microrel.2009.03.009>
15. B. Hu, J. Ortiz Gonzalez, L. Ran, H. Ren, Z. Zeng, W. Lai, B. Gao, O. Alatise, H. Lu, C. Bailey, P. Mawby, Failure and reliability analysis of a SiC power module based on stress comparison to a Si device. *IEEE Trans. Device Mater. Reliab.* **17**, 727–737 (2017). <https://doi.org/10.1109/TDMR.2017.2766692>
16. K.S. Siow, Are sintered silver joints ready for use as interconnect material in microelectronic packaging? *J. Electron. Mater.* **43**, 947–961 (2014). <https://doi.org/10.1007/s11664-013-2967-3>
17. S. Menon, E. George, M. Osterman, M. Pecht, High lead solder (over 85%) solder in the electronics industry: RoHS exemptions and alternatives High lead solder (over 85%) solder in the electronics industry : RoHS exemptions and alternatives. *J. Mater. Sci. Mater. Electron.* (2015). <https://doi.org/10.1007/s10854-015-2940-4>
18. E. George, M. Pecht, Microelectronics reliability RoHS compliance in safety and reliability critical electronics Cost reliability. *Microelectron. Reliab.* **65**, 1–7 (2016). <https://doi.org/10.1016/j.microrel.2016.07.150>
19. S. Sakamoto, S. Nagao, K. Sugauma, Thermal fatigue of Ag flake sintering die-attachment for Si / SiC power devices. *J. Mater. Sci.* **24**, 2593–2601 (2013). <https://doi.org/10.1007/s10854-013-1138-x>
20. C. Chen, K. Sugauma, Microstructure and mechanical properties of sintered Ag particles with flake and spherical shape from nano to micro size. *Mater. Des.* **162**, 311–321 (2019). <https://doi.org/10.1016/j.matdes.2018.11.062>
21. M.S. Kim, H. Nishikawa, Silver nanoporous sheet for solid-state die attach in power device packaging. *Scr. Mater.* **92**, 43–46 (2014). <https://doi.org/10.1016/j.scriptamat.2014.08.010>

22. Y. Yamada, Y. Takaku, Y. Yagi, Y. Nishibe, I. Ohnuma, Y. Sutou, R. Kainuma, K. Ishida, Pb-free high temperature solders for power device packaging. *Microelectron. Reliab.* **46**, 1932–1937 (2006). <https://doi.org/10.1016/j.microrel.2006.07.083>
23. K. Sukanuma, S. Sakamoto, N. Kagami, D. Wakuda, K.S. Kim, M. Nogi, Low-temperature low-pressure die attach with hybrid silver particle paste. *Microelectron. Reliab.* **52**, 375–380 (2012). <https://doi.org/10.1016/j.microrel.2011.07.088>
24. C. Chen, K. Sukanuma, T. Iwashige, K. Sugiura, High-temperature reliability of sintered microporous Ag on electroplated Ag, Au, and sputtered Ag metallization substrates. *J. Mater. Sci. Mater. Electron.* **0**, 0 (2017). <https://doi.org/10.1007/s10854-017-8087-8>
25. R. Khazaka, L. Mendizabal, D. Henry, Review on joint shear strength of nano-silver paste and its long-term high temperature reliability. *J. Electron. Mater.* **43**, 2459–2466 (2014). <https://doi.org/10.1007/s11664-014-3202-6>
26. J. Yan, G. Zou, A.P. Wu, J. Ren, J. Yan, A. Hu, Y. Zhou, Pressureless bonding process using Ag nanoparticle paste for flexible electronics packaging. *Scr. Mater.* **66**, 582–585 (2012). <https://doi.org/10.1016/j.scriptamat.2012.01.007>
27. Z. Zhang, C. Chen, Y. Yang, H. Zhang, D. Kim, T. Sugahara, S. Nagao, K. Sukanuma, Low-temperature and pressureless sinter joining of Cu with micron / submicron Ag particle paste in air. *J. Alloys Compd.* **780**, 435–442 (2019). <https://doi.org/10.1016/j.jallcom.2018.11.251>
28. C. Pei, C. Chen, K. Sukanuma, G. Fu, Thermal stability of silver paste sintering on coated copper and aluminum substrates. *J. Electron. Mater.* **47**, 811–819 (2018). <https://doi.org/10.1007/s11664-017-5857-2>
29. H. Zhang, C. Chen, S. Nagao, K. Sukanuma, Thermal fatigue behavior of silicon-carbide-doped silver microflake sinter joints for die attachment in silicon/silicon carbide power devices. *J. Electron. Mater.* **46**, 1055–1060 (2017). <https://doi.org/10.1007/s11664-016-5069-1>
30. S. Kraft, A. Schletz, M. März, Reliability of silver sintering on DBC and DBA substrates for power electronic applications, in: 2012 7th International Conference on Integration of Power Electronics (CIPS) (2012), pp. 1–6. http://ieeexplore.ieee.org/xpls/abs_all.jsp?arnumber=6170661
31. V.R. Manikam, K.Y. Cheong, Die attach materials for high temperature applications: a review, components, packag. manuf. technol. Packag. Manuf. Technol. *IEEE Trans.* **1**, 457–478 (2011). <https://doi.org/10.1109/TCPMT.2010.2100432>
32. S. Ri, M. Saka, Diffusion—fatigue interaction effect on hillock formation in aluminum thin films under thermal cycle testing. *Mater. Lett.* **79**, 139–141 (2012). <https://doi.org/10.1016/j.matlet.2012.03.109>
33. J.Z. Lu, K.Y. Luo, Y.K. Zhang, C.Y. Cui, G.F. Sun, J.Z. Zhou, L. Zhang, J. You, K.M. Chen, J.W. Zhong, Grain refinement of LY2 aluminum alloy induced by ultra-high plastic strain during multiple laser shock processing impacts. *Acta Mater.* **58**, 3984–3994 (2010). <https://doi.org/10.1016/j.actamat.2010.03.026>
34. R.D. Doherty, R.W. Cahn, Nucleation of new grains in cold worked metals. *J. Less Common Met.* **28**, 279 (1972)
35. M. Reihanian, R. Ebrahimi, N. Tsuji, M.M. Moshksar, Analysis of the mechanical properties and deformation behavior of nanostructured commercially pure Al processed by equal channel angular pressing (ECAP). *Mater. Sci. Eng. A* **473**, 189–194 (2008). <https://doi.org/10.1016/j.msea.2007.04.075>

Publisher's Note Springer Nature remains neutral with regard to jurisdictional claims in published maps and institutional affiliations.